Fusible alloy 'in-contact' microelectrodes: a rapid and economic microfabrication alternative for microfluidic impedance cytometry

Jatin Panwar[1] and Rahul Roy[1,2,3#]

[1]Department of Chemical Engineering, [2]Centre for BioSystems Science and Engineering, [3]Molecular Biophysics Unit, Indian Institute of Science, Bangalore, India

[#]Correspondence:

Rahul Roy
Department of Chemical Engineering,
Indian Institute of Science, Bangalore,
Karnataka, India 560012
Telephone: +91-8022933115;
Fax: +91-8023608121
Email: rahulroy@iisc.ac.in;
rahulfx16@nanobiophotonics.org

Running title:
Fusible alloy 'in-contact' microelectrodes

Keywords:
Microfabrication, Microelectrodes, Microfluidic impedance cytometry, Single cell analysis, Microdroplets.

Manuscript details:
Title – 117 characters; Short title – 39 characters; Abstract – 169 words; Text – 3400 words; Figures – 6; References – 59

Abstract:

Microfluidic impedance cytometry (MIC) provides a fast and label-free method for single cell detection and classification. However, the cost and complexity of MIC electrode fabrication limits its implementation in disposable devices for point-of-care (PoC) applications. To address this, we demonstrate the fabrication and characterisation of Field's metal (FM) 'in-contact' coplanar (icFM) microelectrodes in multilayer elastomer devices and characterise them for microfluidic impedance cytometry. These microelectrodes are fabricated by suction driven molten alloy flow into precast microchannels. After solidification, this electrode layer is bonded to other flow microchannel layer(s) to integrate fluidic operations. Our approach bypasses the conventional clean-room intensive microelectrode fabrication processes and requires a single photolithography step. In a feedback controlled suction-flow MIC setup, our icFM microelectrodes displayed comparable performance to the platinum electrodes in the detection of single human erythrocytes and water-in-oil droplets. Additionally, our microelectrodes can detect single cells entrapped in water-in-oil droplets, an integral operation in droplet based single cell analysis. Thus, fusible alloy microelectrodes provide a facile and cost-effective alternative for impedance flow cytometry.

Introduction :

Microfluidics allows precise control over chemical and biological investigations at micron scales that are comparable to the dimensions of the biological cell. Microfluidic detection and analysis of single cells in lab-on-chip devices has seen a tremendous rise over the years.[1-7] In most microfluidic applications, cell detection is achieved using optical methods. Sensitive methods like fluorescence can allow molecule-specific detection enabling cell classification and sorting. However, these methods require additional labelling steps.[8, 9] Therefore, there have been parallel efforts to develop label-free assays for the detection and characterisation of cells.[10-13]

One such promising technique for single cell analysis is Microfluidic Impedance Cytometry (MIC) which relies on cellular electrical impedance.[14, 15] The dielectric properties of a biological cell are defined by cellular characteristics like cell volume, composition and architecture. Continuous flow microfluidic devices with embedded microelectrodes for electrical measurements can be employed for detecting and classifying single cells in a high throughput manner.[15-19] In current versions of MIC, as the cell suspended in an electrolyte flows over an array of metal electrode pairs connected to a high frequency AC excitation source, the dielectric properties of the media between the electrodes change. This in turn attenuates the measured impedance at a particular frequency across the microelectrode pair and generates a voltage signal. Highly sensitive MIC based detection is already showing promise in characterisation of sub-cellular features.[15, 16, 20]

However, MIC devices rely on cleanroom intensive techniques like metal sputtering and /or vapour deposition to generate metal electrodes on substrates (glass or silicon wafer). The substrate is then bonded to the flow channel to complete the assembly of a coplanar microelectrode integrated microchannel.[21-23] This elaborate and costly microelectrode fabrication process has limited the deployment of MIC in diagnostics and real-world applications.

There have been several prior efforts to develop cheaper and efficient embedded microelectrodes. For example, fusible alloy or liquid metal can be filled into dedicated

microchannels placed in proximity with flow-channels to act as non-contact electrodes.[24, 25] However, these electrodes have limited impedance sensitivity because of the attenuated charge density and electric field strength between the electrodes with the intervening elastomer. As impedance sensitivity has a strong dependence on electrode dimensions and displays optimum sensitivity for electrode widths comparable to the particle size,[26, 27] fabrication of microelectrodes and their placement in close proximity to flow channels is critical for MIC. To address this, alternate architecture(s) where the electrodes are in direct contact, namely, 'in-contact' with the flow channel are employed.[28-30] However, the applicability and consistency of such alternate embedded microelectrodes for impedance detection of single cells and their performance relative to conventional electrodes has not been characterised previously.

In this work, we present a simple fabrication method and characterisation of MIC compatible coplanar 'in contact' Field's metal (icFM) microelectrodes. Our icFM microelectrodes displayed impedance signal strengths and contrast that is comparable to the conventional platinum electrodes for single erythrocyte detection in a custom-built suction driven continuous flow setup. Additionally, icFM microelectrodes show excellent ability to detect cells within water-in-oil microdroplets, a requirement for many single cell isolation and analysis platforms.[31-33] Therefore, we propose icFM microelectrodes as a low-cost and disposable alternative to conventional metal electrodes for microfluidic impedance cytometry.

Materials and Methods:

Electrode fabrication: Microchannels for the flow and the microelectrode layers were designed and fabricated using standard soft photolithography methods.[34, 35] Briefly, microchannels were designed using CleWin 4 and the chrome mask was etched using a mask writer (Heidelberg µPG 501) and EVG 620 was used for UV exposure. Polydimethylsiloxane or PDMS (184 Sylguard, Dow Corning) was used for all the device fabrications. SU8 2015 (MicroChem) was spin-coated on a silicon wafer at 2100 rpm to a thickness of 20 µm prior to UV exposure and development. A PDMS cast of the electrode layer (EL, ~ 4 mm) consisted of three independent 100 µm channels that reduced to 30 µm width and an inter-electrode gap of 20 µm at the detection region (**Figure 1a**). EL also incorporates all inlet and corresponding outlet ports for molten alloy flow as well as fluid flow. A thin (unpatterned) PDMS sacrificial base layer (SL, ~ 1 mm) was placed under EL to close the channels while taking care to remove all trapped air bubbles between elastomer layers. The flexibility and low surface roughness of polymerised PDMS provided an excellent airtight seal between the layers. The EL+SL assembly was placed on a hot plate at 130 °C for 20 mins. 15 µl of molten FM (melting point ~ 60 °C, Bombay metal house) at 130 °C was pipetted into the electrode channel inlets of the assembly while placed on the hot plate. Using a 50 ml syringe, a suction pressure (~ 80 kPa) was applied to the channel until the metal reached the outlet port for each electrode channel. Suction pressure drives the molten alloy flow through the microchannels as well as holds the two layers together without any additional requirements for bonding. The assembly was allowed to cool after scraping off the excess metal till the FM solidified and the SL was peeled off to expose the microelectrodes (**Figure 1a**). The flow layer (FL, 1-4 mm) consisted of a 20 µm high and 70 µm wide channel converging to a 20 µm width at the detection region and runs orthogonally to the electrode channels. In case of water-in-oil droplet measurements, a T-junction was added to the flow channel upstream of the

detection region. EL and FL were aligned using the guide marks and bonded after a plasma treatment. The bottom layer (FL) was also plasma bonded to a glass slide for device rigidity and ease of operation. To overcome the reduced hydrophobicity of the PDMS after plasma treatment, the device was kept overnight in an oven at 45 °C. The device thus fabricated, contains a fluidic channel passing under an array of three 'in-contact' coplanar microelectrodes (**Figure 1b**). Pt electrodes (100 nm thick; 30 µm wide) on glass substrate (MicroX Labs) were assembled in identical microchannels for comparison.

Microfluidic Impedance Cytometry setup: A lock-in amplifier with a built-in signal generator (either HF2LI, Zurich Instruments or CytoX, MicroX Labs) was connected to the microelectrodes via a custom-made low noise instrumentation amplifier circuit. We used the common MIC electrode architecture with three coplanar electrodes within the microfluidic chip representing two electrode pairs[36-38]. An excitation AC signal was applied to the source electrode (middle) via the signal-output port of the lock-in amplifier. The two measuring electrodes (on either side) were connected to the instrumentation amplifier circuit (**Figure 2a**).

Particles passing over the electrodes perturb the dielectric properties (and hence the impedance) of the sample between the electrodes (**Figure 2b**). This change is measured as a voltage offset across the two electrode pairs ($\Delta V = |V_2 - V_1|$). This offset is the signature of the passing particle but is usually too small to be measured directly. The instrumentation amplifier converts the offset voltage from the electrode pairs into a differential voltage (V_{out}) with a gain ($1 + 2R_{gain}/R$), which was then fed into the signal-input of the lock-in amplifier. The amplified differential voltage (Vrms) from the lock-in amplifier was recorded using a software interface (ZiControl or CytoX).

Fluidics: Suction pressure was stabilised using a custom-built active-feedback pressure control module. Suction is provided by a syringe drawn by a syringe pump (1010X, New Era) and is measured by MP3V5050V pressure transducer via NI USB 6008 data acquisition card. A LabVIEW based user interface was designed to monitor and stabilise the applied suction pressure to a desired set point (0-50 kPa) by an active-feedback control of the suction volume. (**Figure 2c**). The control module facilitates application of suction microfluidics[39] in long-term flow management in multi-phase microfluidic devices and thus reduces the control requirements and operation costs.

We used a T-junction flow channel architecture for water-in-oil droplet generation.[40] The continuous phase consisted of fluorinated oil (1863005, Bio-Rad) with cell suspension in 1X Phosphate-buffered saline or PBS (Sigma-Aldrich) as the dispersed phase. The electrolyte concentration was selected to ensure compatibility with potential downstream biochemical reactions and long-term viability of cells in the droplets. The capillary number for the continuous phase and Reynolds number at the T-junction were 8.24×10^{-2} (transient regime)[40] and 0.15, respectively. Droplet of ~ 150 pl volume were generated at a frequency of ~ 10 Hz using 18 kPa suction pressure.

Imaging and analysis: The device images were acquired using a brightfield inverted microscope (RAMM, Applied Scientific Instrumentation). High speed fluorescence imaging for particle velocity profiling was done using a sCMOS camera (Orca Flash 4, Hamamatsu) and green fluorescent protein (GFP) expressing *E. coli* cells were used as fluorescent particles. Images were acquired

using µManager 2.0.[41] Scanning electron microscope (Ultra 55 FE-SEM, Carl Zeiss) was used for electrode surface micrographs. All the data analysis was done using custom codes in MATLAB.

Sample preparation: The blood samples were provided by the author and drawn at the Health center, IISc Bangalore. For erythrocyte enrichment, 5 ml of blood was spun at 500 x g for 7 mins. The supernatant was discarded and the pellet was resuspended in 5 ml of 10X PBS (or 1X PBS in case of droplets). The samples thus prepared were visually inspected using a brightfield microscope (**Figure S1**).

Results and discussion:

Our MIC microfluidic module uses a single standard photolithography workflow to generate two PDMS microchannel layers, i.e. the microelectrode layer (EL) and the flow layer (FL) (**Figure 1**). First, the electrodes are fabricated separately by filling the EL microchannels with a fusible alloy (FM). The channel architecture helps define the arrangement, dimensions and the position of the microelectrodes. We chose FM (32.5% Bi, 51% In, 16.5% Sn) among the eutectic fusible alloys due to its non-toxic nature and melting point of ~ 60 °C which is significantly above room temperature. The flow and electrode layer (with electrodes placed orthogonal to flow channels) are bonded to finish the icFM device assembly. Most of this fabrication workflow is cleanroom independent thus significantly reducing processing time and resource requirements (**Supplementary Table ST1**). Deployment of thus fabricated icFM microfluidic device in a MIC setup with an active feedback pressure control module is described in the Methods and **Figure 2**.

We first confirmed the stability of our feedback pressure control module by monitoring suction pressures at different set points between 5 to 30 kPa across the flow channel filled with distilled water. We observed a steady pressure drop using our control module (standard deviation ± 0.1 %) as compared to a rapidly decaying pressure difference for a non-feedback operation (**Figure 3a**). We also determined the linear relationship between the flow velocity at the detection region and the suction pressure applied across our flow channels which is used to define the particle flow velocities over the electrodes (**Figure 3b**).

We characterised our icFM microelectrode response (Vrms) for different electrolyte concentrations (0 to 10X PBS) at various AC source frequencies (0.1 – 10 MHz) and peak-to-peak source voltages (0.2 to 2 Vp-p) to optimise the applied voltage, source frequency and electrolyte concentration for MIC electrode performance and stability. Ideally, the differential voltage (Vrms) between the measuring electrodes should be zero when placed identically on either sides of the source electrode under similar electrochemical conditions. However, the non-zero differential voltage observed in real-world MIC setups arise from the asymmetry in the electronic system and the system noises and offsets. We relied on the continuity and linearity of the differential signal to evaluate our electrode stability since breakdown in electrode operation will result in discontinuous response. First, we measured the mean Vrms response of the electrodes for electrolyte concentrations from 1X to 10X PBS over a broad frequency range (0.5-10 MHz) at 2 Vp-p. We observed a continuous and monotonically increasing Vrms as a function of electrolyte concentration which suggests that the electrodes are not undergoing electrolysis (**Figure 3c**). Importantly, we observed a linear Vrms output with increasing Vp-p (0- 2 V; 10X PBS) which confirms that these electrodes are electrochemically stable with no corrosion at high saline concentrations[42] up to 2 Vp-p and the linearity can be extrapolated to even

higher source voltages suggesting a wider operable range (**Figure 3d**). Using a frequency sweep (0.1 – 10 MHz; at 2 Vp-p and 10X PBS), we observed a continuous but non-linear impedance response (**Figure 3e**). This could arise because of capacitive coupling at higher frequencies for our electrodes.[43] Frequency dependence of either the double layer capacitance[44] or instrumentation amplifier gain can also result in such a behaviour.

To demonstrate the icFM microelectrode compatibility with MIC and compare its performance with the popular Pt electrodes (in the same coplanar configuration), we detected human erythrocytes (Red Blood Corpuscles or RBC). A suction pressure of 10 kPa maintained the sample at a mean velocity of ~ 15 mm/sec over the electrodes (**Figure 3b**) that was optimised for a sampling rate of 7200 Hz. The differential impedance signature of an erythrocyte in the electrolyte as it flows over the microelectrode array is characteristic of a well-described single 'sine-wave' shape in this configuration (**Figure 4a**).[36] The observed variability in signal peak distribution (as evident from the error bars) arises as a result of variable distance of the flowing cells from the electrodes and inherent cell size dispersity (**Figure 4b**). A comparison of icFM and Pt electrodes in equivalent configuration demonstrates a marginally higher peak signal variability for icFM electrodes. Nevertheless, the peak signal values registered by icFM electrodes were comparable to Pt electrodes. While Pt electrodes displayed a gradual drop in RBC signal over frequencies from 0.5 to 4 MHz, the icFM electrodes were characteristic of a biphasic response with the highest peak signals obtained at 0.5 MHz and 3 MHz. The frequency response is also a function of the biophysical and morphological properties of the cell (and subcellular components like vacuoles and nucleus) and can be used for cell classification on the basis of size, cytoplasmic resistance and membrane capacitance.[16] However, we have limited our analysis to demonstrate proof-of-principle cell detection capability using icFM electrodes in this study. A comparison of signal-to-noise ratios (SNR) also displayed high SNR for both electrodes over the entire frequency range measured (**Figure 4c**). In spite of electrical noises and a comparatively rough surface of the solidified alloy over sputtered metal (**Figure S2**), the performance of both electrodes was similar within the accounted parameters. Hence, icFM electrodes can be a viable alternative for MIC based single cell detection.

Next, we integrated icFM electrodes to detect water-in-oil droplets, a common two-phase microfluidic configuration used as microreactors.[45] By employing elastomeric walls on all four sides, the microchannels in our devices exhibit uniform hydrophobicity which aids droplet microfluidic operations.[46] Droplets (1X PBS) were generated using a T-junction upstream of the microelectrodes. The signal for aqueous droplets is characteristic of a high dielectric feature in a continuous oil phase flowing through the channel (**Figure 5a**). Comparison of the distribution of peak heights and corresponding full width at half maxima or FWHM for erythrocytes and droplets in oil revealed features of the two flow profiles (**Figure 5b**). The FWHM is a function of the residence time of the particle in the detection region. A large standard deviation of the FWHM for the RBC (11.73 %) results from the parabolic flow profile within the microchannel. The RBC peak heights also have a substantially larger standard deviation (24.68 %) because of the variable normal distance of the cells from the electrodes apart from the inherent cell size heterogeneity and tumbling of the RBC in the channel. On the other hand, droplets show significantly narrow distribution of peak heights (1.92 %) and FWHM (1.84 %) as a result of the plug flow profile of the droplets. The

distribution in the droplet signal also agrees well with the polydispersity of the droplet plug length (1.69 %) as calculated using brightfield microscopy (**Figure S3**). We also observed an excellent overlap in the primary peak height distribution for the droplets over time (~ 60 mins) even after continuous measurements on the same device (**Figure 5c**). This suggested the long-term stability of the icFM electrodes in such two phase systems.

Cell entrapment in droplets is an increasingly popular single cell analysis tool.[47, 48] However, high-throughput quantification of entrapped cells usually relies on high-speed optical imaging. Non-optical methods to detect and quantify cells in microdroplets can aid in challenges with sensitivity and the requirement to label the cells.[49] To demonstrate the applicability of icFM electrodes for quantitative single cell detection in microdroplets, we performed MIC measurements of erythrocytes in droplets (**Figure 6a**). We hypothesised that an additional set of secondary signatures superimposed on the droplet signal will be discernible if the droplet contained cell(s) owing to its membrane capacitance (**Figure 6b**). Since the cytoplasm is shielded by the low dielectric of the cell membrane at frequencies below 10 MHz, its cytoplasmic conductivity does not contribute to an impedance change in our measurements. Therefore, the cell-in-droplet signal would be defined by a low dielectric feature (cell) suspended in a high dielectric medium (droplet) as its travels in a low dielectric carrier phase (oil). Thus, a cell in a droplet is expected to display an overlay of the cell signature on the droplet signal resulting in primary and secondary peaks (**Figure 6b**).[16] The primary and the secondary peak reach their corresponding maxima when the contributor (droplet and cell in droplet, respectively) passes directly over the center of the source and measuring electrode. This idea can be further explained by an equivalent electrical circuit model (**Figure 6c**).[50] The centered droplet would contribute the maximum differential impedance owing to its highest conductivity (1.6 S/m) and relative permittivity (80 for 1X PBS) compared to the carrier phase and the cell (**Figure 6c**). The MIC signal for our erythrocytes in droplets indeed displayed secondary peaks consistent with the average number of cells loaded per droplet (**Figure 6d**). To statistically validate our cell quantification, we calculated the fraction of droplets with one or more RBC counts from the number of secondary peaks at different dilutions of our erythrocyte suspension (**Figure 6e**). Physical overlap of cells over the detection region should not contribute to large discrepancies in our peak based analysis at low cell densities. The observed total RBC counts at each dilution was consistent with estimates (5 x 10^9 RBCs/ml of human blood) when accounted for the offset attributed to RBC loss during sample preparation (**Figure 6f**). This further demonstrated the sensitivity of our icFM microelectrodes for detection of particles in complex two-phase microfluidic systems.

Conclusion:

We have demonstrated Field's metal based 'in-contact' (icFM) microelectrodes as a rapid and economical alternative for single cell detection. We present a technically simple fabrication process that produces highly reproducible MIC microelectrodes in a cleanroom-free environment. Our microelectrodes are robust in all solution conditions used for conventional cell analysis and comparable in performance to metal electrodes[15]. This allows us to monitor cells in water-in-oil droplets non-optically with high contrast. Incorporation of non-conductive flow focusing or sheath flow to reduce the detection volume can be further employed with icFM devices to achieve higher sensitivity.[51, 52] Two opposing icFM electrode

layers sandwiching a flow layer in 3D electrode geometry can further improve the MIC signal strength, thus enabling more challenging applications like cell classification and bacteria detection.[16]

While our fabricated microelectrodes were designed and characterised for MIC, which places high technical requirements for performance, we also envision their application in AC electrokinetics, electrochemical sensing, microfluidic mixing and sorting. [53-58] As the casting is done directly within the prefabricated devices, the process is compatible with other polymeric materials.[59] With possibility of scaling up the microfabrication process with automation, use of these electrodes in disposable PoC devices can become a reality.

Conflicts of interest:

There are no conflicts to declare.

Acknowledgements:

This project was partially funded by support from the Indian Institute of Science (IISc) Bangalore, Wellcome Trust – DBT India Alliance and Rao Biomedical Research Fund. We thank Prosenjit Sen and Karthik Mahesh, Center for Nano Science and Engineering (CeNSe),IISc for providing their MIC setup and MicroX Labs, Bangalore for providing their integrated lock-in amplification FPGA board and Pt electrodes along with Logic-fruit technologies for technical support. We acknowledge use of the lithography facilities at the CeNSe, funded by the Department of Information Technology, Gov. of India. We also thank Abhishek Ranade for SEM; Priyanka V. and Satyaghosh Maurya for their support in device fabrication and data analysis, respectively and Lakshmi Supriya, Prithiv Natarajan and Suraj Jagtap for their inputs on the manuscript.

References:

1. M. Mehling and S. Tay, *Current Opinion in Biotechnology*, 2014, **25**, 95-102.
2. A. M. Streets, X. Zhang, C. Cao, Y. Pang, X. Wu, L. Xiong, L. Yang, Y. Fu, L. Zhao, F. Tang and Y. Huang, *Proceedings of the National Academy of Sciences*, 2014, **111**, 7048.
3. A. Reece, B. Xia, Z. Jiang, B. Noren, R. McBride and J. Oakey, *Current opinion in biotechnology*, 2016, **40**, 90-96.
4. W. Jung, J. Han, J.-W. Choi and C. H. Ahn, *Microelectronic Engineering*, 2015, **132**, 46-57.
5. David J. Beebe, a. Glennys A. Mensing and G. M. Walker, *Annual Review of Biomedical Engineering*, 2002, **4**, 261-286.
6. H.A. Stone, a. A.D. Stroock and A. Ajdari, *Annual Review of Fluid Mechanics*, 2004, **36**, 381-411.
7. Q. Shi, L. Qin, W. Wei, F. Geng, R. Fan, Y. Shik Shin, D. Guo, L. Hood, P. S. Mischel and J. R. Heath, *Proceedings of the National Academy of Sciences*, 2012, **109**, 419-424.
8. E. A. Specht, E. Braselmann and A. E. Palmer, *Annual Review of Physiology*, 2017, **79**, 93-117.
9. A. Ettinger and T. Wittmann, in *Methods in Cell Biology*, eds. J. C. Waters and T. Wittman, Academic Press, 2014, vol. 123, pp. 77-94.
10. J. V. Watson, *Introduction to Flow Cytometry*, Cambridge University Press, Cambridge, 1991.
11. T. Blasi, H. Hennig, H. D. Summers, F. J. Theis, J. Cerveira, J. O. Patterson, D. Davies, A. Filby, A. E. Carpenter and P. Rees, *Nature Communications*, 2016, **7**, 10256.
12. M. G. Kim, J. Park, H. G. Lim, S. Yoon, C. Lee, J. H. Chang and K. K. Shung, *Scientific Reports*, 2017, **7**, 14092.
13. H. M. Shapiro, in *Practical Flow Cytometry*, John Wiley & Sons, Inc., 2005, DOI: 10.1002/0471722731.ch6, pp. 257-271.
14. D. Holmes and H. Morgan, *Analytical Chemistry*, 2010, **82**, 1455-1461.

15. M. Hywel, S. Tao, H. David, G. Shady and G. G. Nicolas, *Journal of Physics D: Applied Physics*, 2007, **40**, 61.
16. T. Sun and H. Morgan, *Microfluidics and Nanofluidics*, 2010, **8**, 423-443.
17. N. N. Watkins, U. Hassan, G. Damhorst, H. Ni, A. Vaid, W. Rodriguez and R. Bashir, *Science Translational Medicine*, 2013, **5**, 214ra170-214ra170.
18. X. Han, C. van Berkel, J. Gwyer, L. Capretto and H. Morgan, *Analytical Chemistry*, 2012, **84**, 1070-1075.
19. W. H. Coulter, 1956.
20. J. S. McGrath, C. Honrado, D. Spencer, B. Horton, H. L. Bridle and H. Morgan, *Scientific reports*, 2017, **7**, 2601.
21. C. E. Chidsey, B. J. Feldman, C. Lundgren and R. W. Murray, *Analytical Chemistry*, 1986, **58**, 601-607.
22. P. K. Kannan, R. V. Gelamo, H. Morgan, P. Suresh and C. S. Rout, *RSC Advances*, 2016, **6**, 105920-105929.
23. Y. Temiz, A. Ferretti, Y. Leblebici and C. Guiducci, *Lab on a Chip*, 2012, **12**, 4920-4928.
24. L. D. Thredgold, D. A. Khodakov, A. V. Ellis and C. E. Lenehan, *Analyst*, 2013, **138**, 4275-4279.
25. A. Sciambi and A. R. Abate, *Lab on a Chip*, 2014, **14**, 2605-2609.
26. C. Clausen, G. Skands, C. Bertelsen and W. Svendsen, *Micromachines*, 2015, **6**, 110.
27. S. Gawad, K. Cheung, U. Seger, A. Bertsch and P. Renaud, *Lab on a Chip*, 2004, **4**, 241-251.
28. J.-H. So and M. D. Dickey, *Lab on a Chip*, 2011, **11**, 905-911.
29. S. H. Song, T. Maleki and B. Ziaie, *CMBS*, 2011, **11**, 4-5.
30. M. T. Guler, I. Bilican, Z. Isiksacan, S. Agan and C. Elbuken.
31. Q. Zhang, T. Wang, Q. Zhou, P. Zhang, Y. Gong, H. Gou, J. Xu and B. Ma, *Scientific Reports*, 2017, **7**, 41192.
32. L. Rosenfeld, T. Lin, R. Derda and S. K. Y. Tang, *Microfluidics and Nanofluidics*, 2014, **16**, 921-939.
33. H. N. Joensson and H. Andersson Svahn, *Angewandte Chemie International Edition*, 2012, **51**, 12176-12192.
34. L. F. Thompson, ACS Publications, 1983.
35. D. C. Duffy, J. C. McDonald, O. J. A. Schueller and G. M. Whitesides, *Analytical Chemistry*, 1998, **70**, 4974-4984.
36. S. Gawad, L. Schild and P. Renaud, *Lab on a Chip*, 2001, **1**, 76-82.
37. V. Errico, A. D. Ninno, F. R. Bertani, L. Businaro, P. Bisegna and F. Caselli, *Sensors and Actuators B: Chemical*, 2017, **247**, 580-586.
38. H. C. Clausen, E. G. Skands, V. C. Bertelsen and E. W. Svendsen, *Micromachines*, 2015, **6**.
39. A. R. Abate and D. A. Weitz, *Biomicrofluidics*, 2011, **5**, 014107.
40. J. H. Xu, S. W. Li, J. Tan and G. S. Luo, *Microfluidics and Nanofluidics*, 2008, **5**, 711-717.
41. A. D. Edelstein, M. A. Tsuchida, N. Amodaj, H. Pinkard, R. D. Vale and N. Stuurman, *Journal of biological methods*, 2014, **1**.
42. S. Zeitler, E. Wendler-Kalsch, W. Preidel and V. Tegeder, *Materials and Corrosion*, 1997, **48**, 303-310.
43. W. Shuo, F. C. Lee, D. Y. Chen and W. G. Odendaal, *IEEE Transactions on Power Electronics*, 2004, **19**, 869-877.
44. K. J. Aoki, *Journal of Electroanalytical Chemistry*, 2016, **779**, 117-125.
45. S.-Y. Teh, R. Lin, L.-H. Hung and A. P. Lee, *Lab on a Chip*, 2008, **8**, 198-220.
46. B. Subramanian, N. Kim, W. Lee, D. A. Spivak, D. E. Nikitopoulos, R. L. McCarley and S. A. Soper, *Langmuir*, 2011, **27**, 7949-7957.
47. H. N. Joensson and H. Andersson Svahn, *Angewandte Chemie International Edition*, 2012, **51**, 12176-12192.
48. M. T. Guo, A. Rotem, J. A. Heyman and D. A. Weitz, *Lab on a Chip*, 2012, **12**, 2146-2155.
49. H. Lu, O. Caen, J. Vrignon, E. Zonta, Z. El Harrak, P. Nizard, J.-C. Baret and V. Taly, *Scientific Reports*, 2017, **7**, 1366.

50. D. Holmes, D. Pettigrew, C. H. Reccius, J. D. Gwyer, C. van Berkel, J. Holloway, D. E. Davies and H. Morgan, *Lab on a Chip*, 2009, **9**, 2881-2889.
51. R. Rodriguez-Trujillo, C. A. Mills, J. Samitier and G. Gomila, *Microfluidics and Nanofluidics*, 2007, **3**, 171-176.
52. C. Bernabini, D. Holmes and H. Morgan, *Lab on a Chip*, 2011, **11**, 407-412.
53. N. Sasaki, T. Kitamori and H.-B. Kim, *Lab on a Chip*, 2006, **6**, 550-554.
54. J. Luo, E. L. Nelson, G. P. Li and M. Bachman, *Biomicrofluidics*, 2014, **8**, 034105.
55. M. Z. Bazant and T. M. Squires, *Physical Review Letters*, 2004, **92**, 066101.
56. A. Ramos, H. Morgan, N. G. Green and A. Castellanos, *Journal of Physics D: Applied Physics*, 1998, **31**, 2338.
57. Z. Nie, C. A. Nijhuis, J. Gong, X. Chen, A. Kumachev, A. W. Martinez, M. Narovlyansky and G. M. Whitesides, *Lab on a Chip*, 2010, **10**, 477-483.
58. D. Chatterjee, H. Shepherd and R. L. Garrell, *Lab on a Chip*, 2009, **9**, 1219-1229.
59. B. Zhang, Q. Dong, C. E. Korman, Z. Li and M. E. Zaghloul, *Scientific Reports*, 2013, **3**, 1098.

Figure 1:

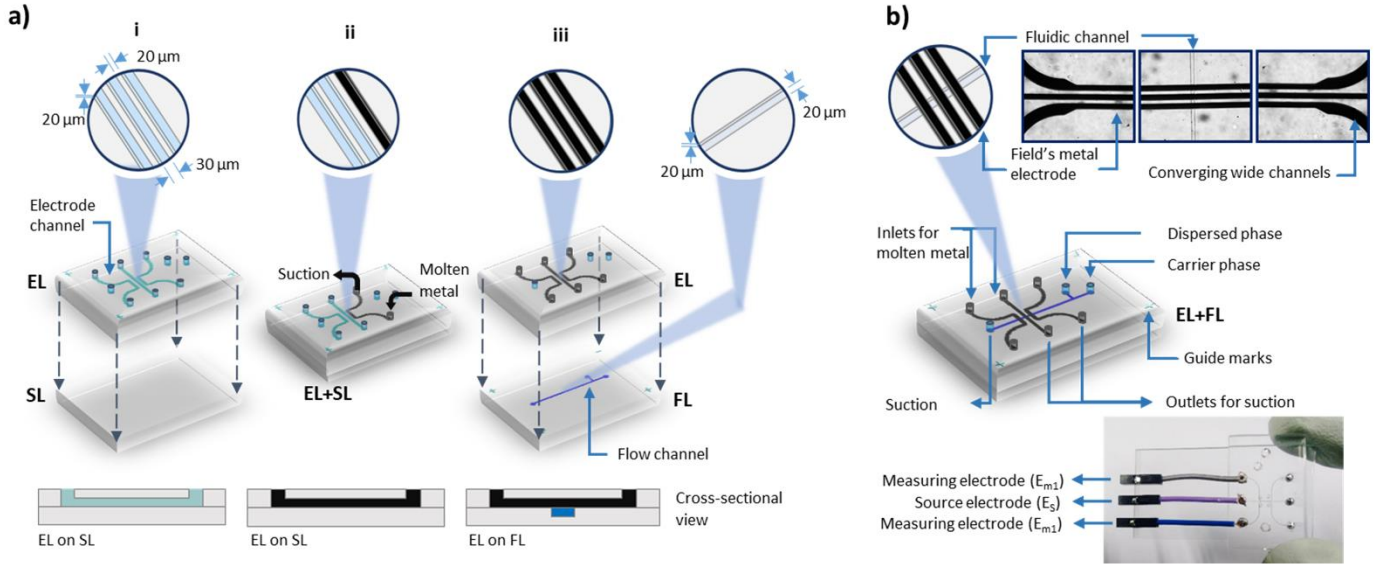

Figure 1: Coplanar 'in-contact' Field's metal (icFM) electrode fabrication workflow **a)** Schematic of fabrication process; **i**: The PDMS layer containing electrode channels (EL) is placed on a flat PDMS sacrificial layer (SL) which acts as a base during electrode casting. **ii**: Molten FM is flown into the electrode channels using suction. SL is peeled off once the electrodes solidified. **iii:** Electrode layer (EL) is then plasma bonded to the flow layer (FL) **b)** Schematic and optical image of the assembled microfluidic device with embedded coplanar icFM microelectrodes is shown.

Figure 2:

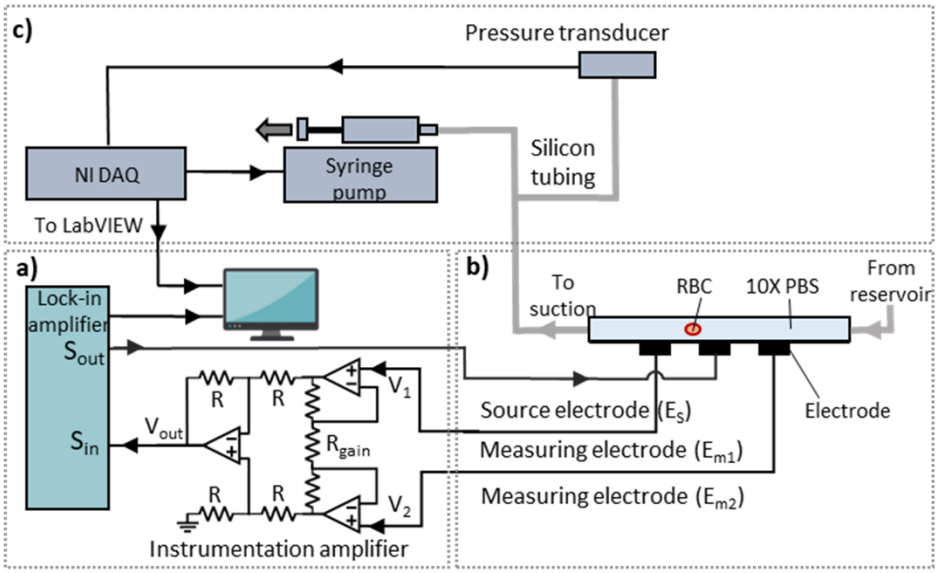

Figure 2: Lock-in amplification based Microfluidic Impedance Cytometry (MIC) setup with feedback controlled suction flow **a)** Lock-in amplifier with built-in signal generator provides the excitation AC voltage (S_{out}) to the source electrode and measures the differential voltage signal (S_{in}) from the measuring electrodes via an instrumentation amplifier. **b)** A cross section of the 'in-contact' coplanar electrodes orthogonal to the flow channel with its fluidic and electronic connections is shown. **c)** Schematic of active feedback pressure control module that regulates suction for fluid flow in the microfluidic channel is drawn.

Figure 3:

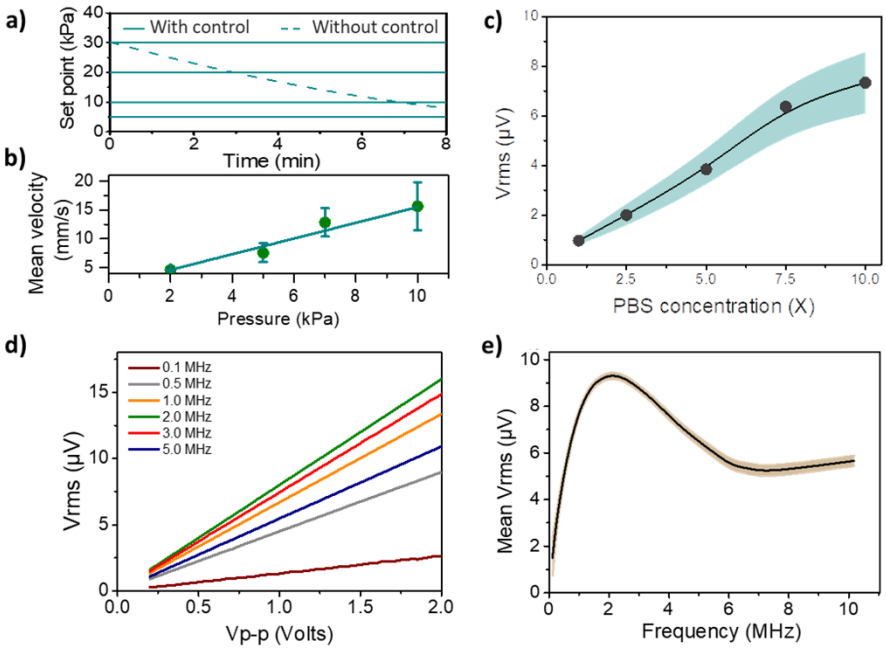

Figure 3: System characterisation **a)** Suction pressure with and without active feedback pressure control module is plotted with time. **b)** Particle velocity over the electrodes as a function of varying suction pressure across the flow channel. **c)** Output voltage (Vrms) measurement for coplanar icFM electrode as a function of electrolyte (PBS) concentration averaged over different source frequencies (0.1 - 10 MHz) at 2 Vp-p is plotted. **d)** Voltage sweep from 0.2 to 2 Vp-p source voltage performed at various frequencies (0.1 - 5MHz) at 10X PBS is shown. **e)** Mean output voltage (Vrms) for frequency sweep (0.1 - 10 MHz) averaged over source voltages (0.5, 1, 1.5, 2 Vp-p) at 10X PBS is reported.

Figure 4:

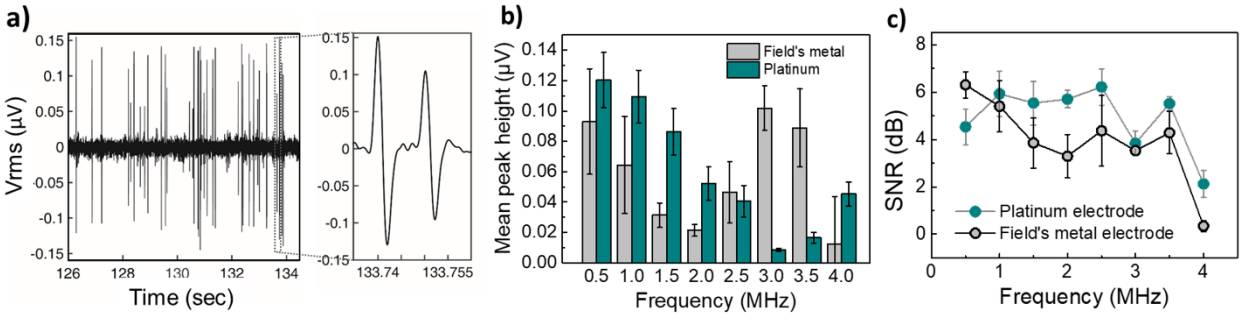

Figure 4: Single erythrocyte detection with coplanar icFM microelectrode **a)** Differential voltage signal from the icFM MIC setup at 2 Vp-p and 0.5 MHz for flowing dilute suspension of RBC in 10X PBS is shown. (Inset) The observed spikes represent a signature waveform for particle detection in our MIC setup, i.e. each positive-negative peak pair representing a single RBC flowing over the electrodes. **b)** Mean peak heights of differential voltage signal for RBC detection obtained using icFM and platinum electrodes at different frequencies at 2Vp-p source voltage is shown. **c)** Comparison of signal-to-noise ratios (SNR) of icFM and platinum electrodes at different frequencies is plotted.

Figure 5:

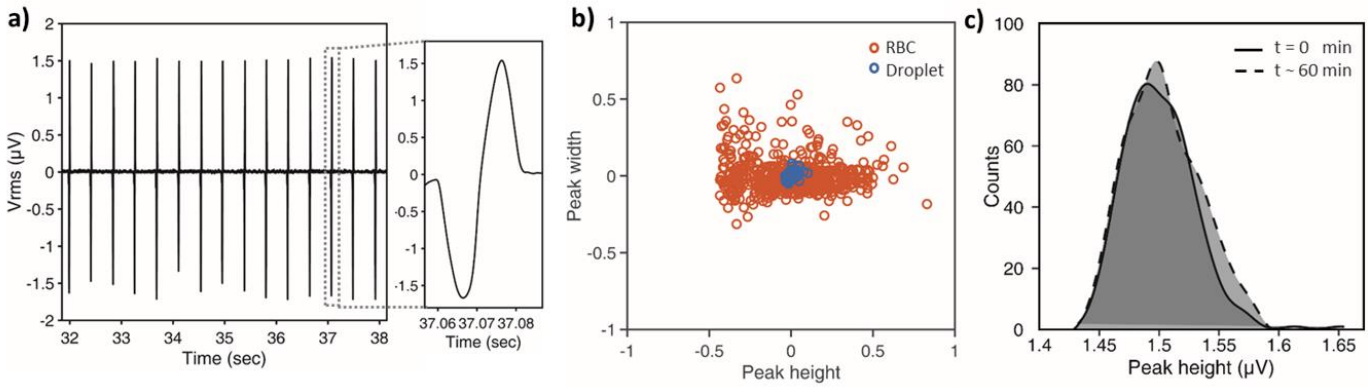

Figure 5: Water-in-oil droplet detection with icFM microelectrode **a)** Differential voltage signal from MIC setup for droplet detection at 2 Vp-p and 1 MHz is shown. (Inset) A zoomed view of the signature waveform for a single droplet detection is displayed. **b)** Comparison of peak height and corresponding FWHM distribution obtained at 2 Vp-p and 1 MHz for RBC and droplet signals is plotted **c)** Peak height distribution for droplet signals from experiments conducted ~ 60 minutes apart on the same device is shown.

Figure 6:

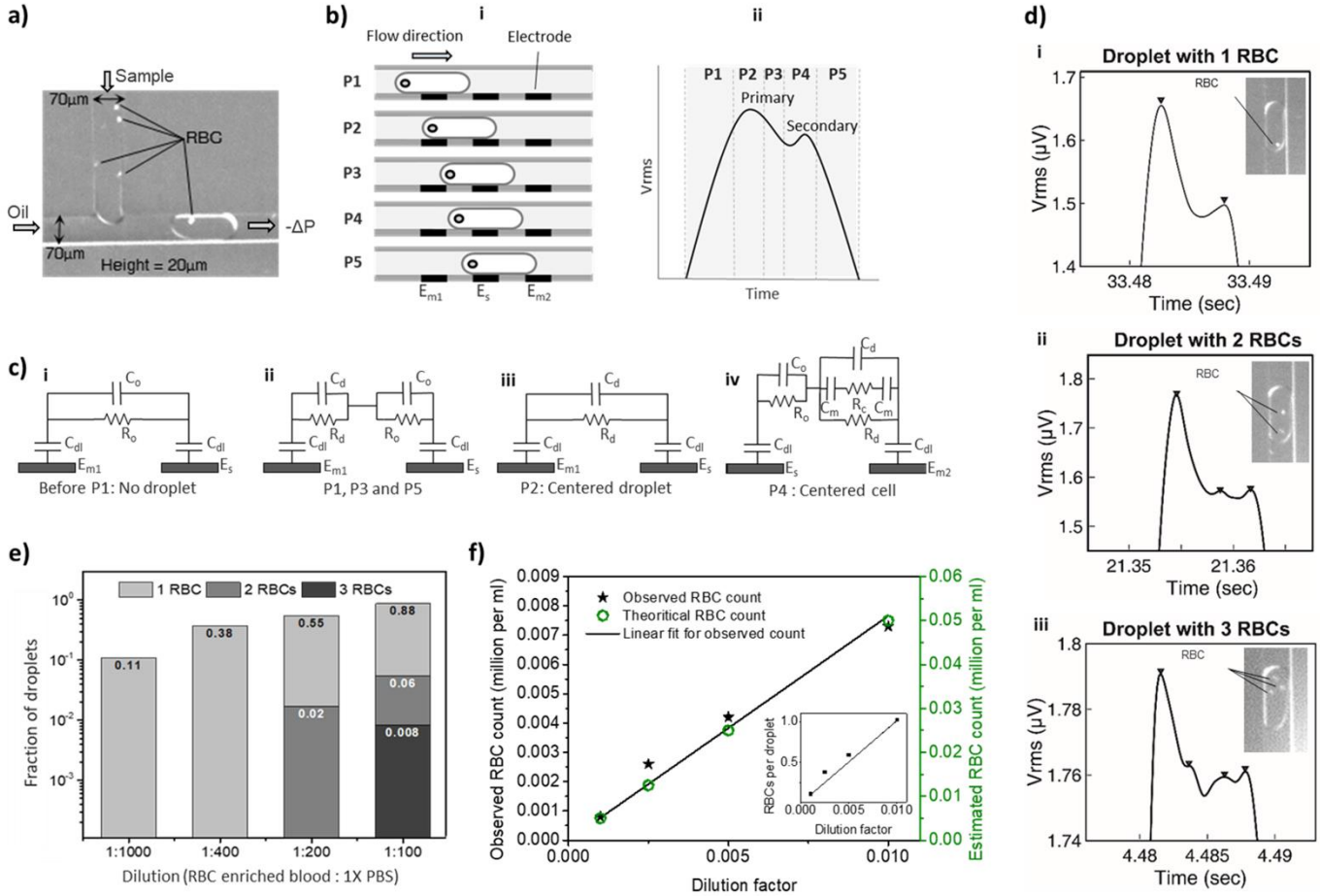

Figure 6: Cell-in-microdroplet quantification **a)** T-junction microfluidic channel used to encapsulate cell(s) in droplets upstream of the microelectrode array is shown. **b)** Schematic representing evolution of primary and secondary peaks for droplet and cell-in-droplet, respectively is depicted **i:** Droplet (containing a single cell) at specific positions relative to the microelectrode array (E_{m1}, E_{m2}: measuring electrodes, E_s: source electrode) is pictorially shown. **ii:** Contribution of each position to differential signal is schematically plotted (only positive peak of differential signal is considered here, the negative peak carries similar features). **c)** Equivalent electrical circuit model for the droplets at different positions is drawn (C_{dl}: equivalent double layer capacitance due to all interfaces (electrode-oil, oil-electrolyte and electrolyte-electrode); C_o, R_o, C_d, R_d: capacitance and resistance due to oil and droplet respectively; C_m: cell membrane capacitance, R_c: cytoplasmic resistance) **i:** Base impedance without droplet, accounting for low conductivity and dielectric constant of carrier phase (Oil). **ii:** As the aqueous droplet touches E_{m1} (and not E_s), the higher dielectric constant of droplet starts to contribute to the signal. **iii:** Primary peak appears as the droplet touches both the electrodes reaching maximum conductivity and dielectric constant between the electrodes. **iv:** Secondary peak appears as the cell crosses the centre of E_s and E_{m1}. **d)** Differential voltage signal at 2 Vp-p and 1 MHz for droplets carrying cells **i-iii:** Primary peak representing a droplet and secondary peaks representing number of entrapped RBCs is plotted. (Inset) Optical image of different droplets containing as many RBCs is shown. **e)** Fraction of droplets encapsulating one, two and three RBCs at represented dilutions is plotted. **f)** Comparison between observed and estimates of total RBC count for each dilution factor is plotted. (Inset) Average number of RBC per droplet as a function of dilution factor is plotted.